University of Ljubljana
Department of Physics
Jadranska 19, 1000 Ljubljana

FLUID FLOWS IN ROTATING FRAMES

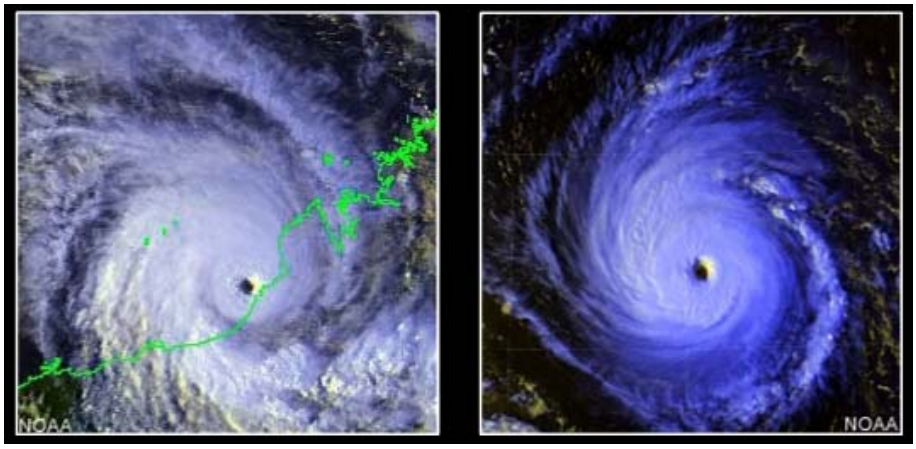

Author: Miha Mežnar

Adviser: dr. Rudolf Podgornik

Ljubljana, 1 March 2005

Contents

Abstract

In my seminar I present the effect of rotating environment on fluid flows. First I show an interesting effect of wind on ocean currents. I than focus on a teacup and explain why particles at the bottom gather in the centre of cup. Finally I show fascinating (stable) patterns that researchers observed during rotating disk experiment and compare the pictures with numerical simulations.

Picture on the front page is from [10]. The storm on the left is in the Southern Hemisphere and the storm on the right is in the Northern Hemisphere.

Figure 1: Spiral galaxy [9].

1 Introduction

Spiral galaxies (Figure 1), atmospheric or oceanic circulation, hurricanes and tornadoes, and, closer to our daily lives, bathtub vortices and stirring tea in a teacup, are all examples of the ubiquity of swirling flows at all scales in nature.

Vortices and rotating flows have fascinated people for centuries. But the description of swirling flows in more than just observational details had to wait for the Navier–Stokes equation. And even then the equation was so difficult to solve, that it had to await the advent of computers and with them numerical solutions.

The fascination continues today. In my seminar I will describe some examples of rotating fluids. I shall begin with the most common rotating frame – the Earth. In this frame I will describe flow of an ocean, driven by a wind (Nansen 1902 and Ekman 1905). Than I shall turn my attention to rotation on a smaller scale. I shall present the "teacup experiment" (Einstein 1926) and afterwards apply some theory, describing the phenomena. At the end of the seminar, I will present latest experiments on fluid flow patterns between rotating disks ([6], [7], [8]).

2 Wind-driven ocean currents

At the end of the XIX-th century the Norwegian oceanographer *Fridtjof Nansen* took part in polar expeditions. In the 1898 expedition he noticed quite a remarkable fact that the iceberg drift was not along the wind direction, as expected, but rather towards the right. Nansen himself was not able to explain this observation theoretically, but Swedish physicist *Walfrid Ekman* was.

Let us follow Ekman's derivation. We start with the *Navier–Stokes equation* for incompressible fluid ($\nabla \cdot \boldsymbol{u} = 0$) [1]:

$$\rho \frac{\partial \boldsymbol{u}}{\partial t} + \rho(\boldsymbol{u} \cdot \nabla)\boldsymbol{u} = -\nabla p + \eta \nabla^2 \boldsymbol{u} + \rho \boldsymbol{f}. \tag{1}$$

In equation ρ is density, $\boldsymbol{u}$ velocity and η viscosity of the fluid, p is pressure and $\boldsymbol{f}$ are external forces per unit mass [N/kg] acting on fluid. In Nansen's case only the last two factors remain. The firs factor vanishes because of the assumption of steady flow, the second because of incompressibility of the fluid ($\nabla \cdot \boldsymbol{u} = 0$) and the third one because there's no pressure gradient (the pressure is constant). Since gravity and centrifugal force only shift the pressure, the only external force present in our problem is the *Coriolis force*. It is defined by

$$\boldsymbol{f} = 2\rho \boldsymbol{u} \times \boldsymbol{\omega}_E, \tag{2}$$

where $\boldsymbol{\omega}_E$ is the angular velocity with which the Earth spins about its axis and ω_E its magnitude.

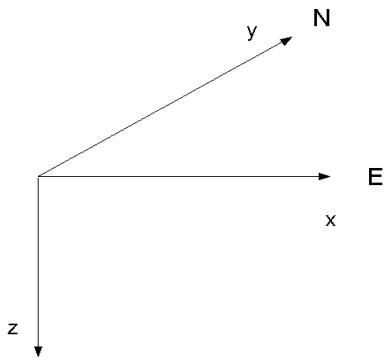

Figure 2: Coordinate system in which the wind-driven ocean flow is described.

We assume a steady, homogeneous and horizontal flow. As a consequence the time and horizontal derivatives are zero $\partial/\partial t = \partial/\partial x = \partial/\partial y = 0$. Therefore the fluid velocity has two components: x-component u_x and y-component u_y, which depend on z-coordinate which is positive downward (increases with depth). From (1) we have

$$\begin{aligned} \eta\frac{\partial^2 u_x}{\partial z^2} + 2\rho\omega_E \sin(\lambda) u_y &= 0 \\ \eta\frac{\partial^2 u_y}{\partial z^2} - 2\rho\omega_E \sin(\lambda) u_x &= 0, \end{aligned} \tag{3}$$

where λ stands for Earth latitude ($\lambda = +\pi/2$ at the north pole and $\lambda = -\pi/2$ at the south pole). In solving set of equations (3) we make use of typical procedure. We first multiply the second equation by imaginary constant $i = \sqrt{-1}$, than add both equations, set $u_x - iu_y = w$ and $2\rho\omega_E \sin\lambda/\eta = \alpha^2$ and we arrive at the equation

$$\frac{\partial^2 w}{\partial z^2} - \alpha^2 w = 0, \tag{4}$$

which has the solution

$$w = w_0 \exp(\pm\alpha z). \tag{5}$$

Since the velocity must diminish with depth, only the negative sign is relevant. Constant α is $\alpha = \pm\sqrt{2\rho\omega_E \sin\lambda/\eta}\sqrt{i} = \pm D(1+i)$, where $D = \sqrt{\rho\omega_E \sin\lambda/\eta}$. [1] We have to take positive α to have finite velocity at great depths. We can now write the solutions:

$$\begin{aligned} u_x &= V_0 \exp(-Dz)\cos(-Dz+\delta) \\ u_y &= V_0 \exp(-Dz)\sin(-Dz+\delta), \end{aligned} \tag{6}$$

where V_0 is the amplitude of velocity and δ another constant which comes from w_0. The constants still have to be evaluated from boundary conditions. Boundary conditions are the components of stress tensor that acts on the surface of the ocean. We take the wind blowing to the north (y-direction). Therefore we only have wind stress that acts in north direction whereas that to the east (x-direction) is zero:

$$\tau_{yz} = -\eta\left(\frac{\partial u_y}{\partial z}\right)_{z=0} = \tau \neq 0 \qquad \text{and} \qquad \tau_{xz} = -\eta\left(\frac{\partial u_x}{\partial z}\right)_{z=0} = 0. \tag{7}$$

From the last equation we get

$$-V_0 D\eta \exp(-Dz)[-\sin(-Dz+\delta) + \cos(-Dz+\delta)]_{z=0} = 0 \quad \Rightarrow \quad \sin\delta = \cos\delta \quad \Rightarrow \quad \delta = \tfrac{\pi}{4} \tag{8}$$

[1] $\sqrt{i} = \sqrt{\exp(i\pi/2)} = \exp(i\pi/4) = \cos\pi/4 + i\sin\pi/4 = \frac{\sqrt{2}}{2}(1+i)$

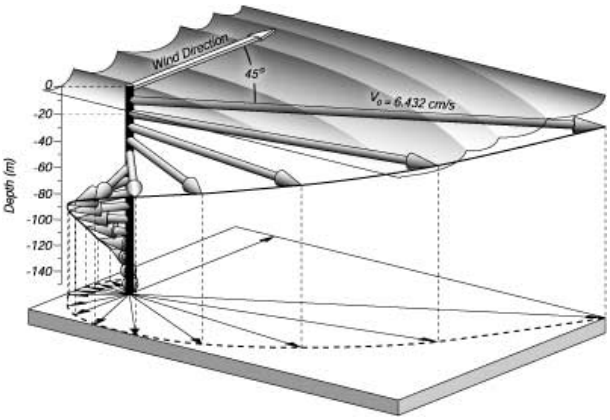

Figure 3: Ekman current generated by a 10 m/s wind at 35 °N [11].

and from the first equation of (7) we get

$$V_0 D\eta \exp(-Dz)[\sin(-Dz+\delta)+\cos(-Dz+\delta)]_{z=0} = \tau \quad \Rightarrow \quad V_0 = \frac{\sqrt{2}\tau}{2D\eta} = \frac{\tau}{\sqrt{2\eta\rho\omega_E \sin\lambda}}. \quad (9)$$

We can see from equation (9) that the amplitude of current velocity is proportional to the effective wind stress τ and inversely proportional to the sine of the latitude. Since the motion in the ocean is turbulent rather than laminar, we substitute "eddy viscosity" A for the normal viscosity η to account for turbulent motion. Eddy viscosity A is typically much greater than η (for water $\eta = 10^{-3}\text{kgs}^{-1}\text{m}^{-1}$ but $A = 10\text{kgs}^{-1}\text{m}^{-1}$). [2] Let us calculate V_0! We assume the wind speed is 10m/s at middle latitudes (35°). At that speed $A = 57.7\text{kgs}^{-1}\text{m}^{-1}$ and we take the wind stress to be $\tau = 0.35\text{Nm}^{-2}$. Inserting these values into equation (9) we get $V_0 = 36\text{cms}^{-1}$ (values for A and τ are taken from [5]).

We just found out (equation (8)) that the ocean surface current flows at 45 ° to the right of the wind when looking downwind in the northern hemisphere. [3] This means that if the wind blows to the north an iceberg will move to the north–east. We can also see from equations (6) that the flow velocity rotates and decays exponentially with depth:

$$u = \sqrt{u_x^2 + u_y^2} = a\exp(-Dz). \quad (10)$$

Figure 3 shows how the flow velocity changes with depth.

The most fascinating thing about the wind driven current is the fact that *total mass transport* is only in the x-direction. [4] The total mass transport is defined as

$$M_x = \int_0^\infty \rho\, u_x \,\mathrm{d}z \qquad \text{and} \qquad M_y = \int_0^\infty \rho\, u_y \,\mathrm{d}z. \quad (11)$$

By inserting the appropriate expressions for velocities u_x and u_y we get

$$M_x = \frac{\tau}{2D^2} = \frac{\tau\eta}{2\rho\omega_E \sin\lambda} \qquad \text{and} \qquad M_y = 0. \quad (12)$$

Therefore the mass of water moves perpendicular to the wind direction. This is quite different from what one would expect at first sight.

Off course our derivation is not valid in every sea. I will therefore summarize the assumptions we made.

[2] The uncertainties in our knowledge of the "effective" wind stress τ and "effective" eddy viscosity coefficients prohibit a thorough comparison of theoretical results with direct observations.

[3] The current is 45 ° to the left of the wind in the southern hemisphere.

[4] We assume the wind blows to the north (y-direction).

Figure 4: Primary and secondary motion in a teacup [12].

1. The ocean has no boundaries. This is valid away from coasts in large oceans.
2. Infinitely deep ocean. This is never really true, but is a good approximation for oceans deeper than 200 m.
3. We assumed steady flow. This is valid only if wind blows in the same direction for at least one day.
4. The approximation of homogeneous density is quite good, though it does change with depth.
5. We assumed that the wind friction is confined to a thin boundary layer and is zero inside the ocean.

3 Swirling flow in a teacup

In this section we shall move towards our everyday life. We have surely all drunk tea. But how many of you asked why do tea leaves (or other small particles heavier than water) collect towards the center of the cup? One would expect at first sight the particles should be expelled outwards by the centrifugal force. It is said that this was exactly the question that teased Mrs. Schrödinger. And it was Albert Einstein who appeased her curiosity, which her husband could not satisfy.

When the tea leaves are rotating around the bottom of a cup, they spiral towards the center of the cup as they follow the motion of the water that was induced by stirring the tea with spoon. They move towards the center after the spoon is removed and, hence, when the water in the cup begins to spin down towards a state of rest. The pressure near the side walls of the cup is higher than the pressure in the center when the water is rotating. This can be observed by the shape of the surface of the water which is concave from the viewpoint of the drinker. This pressure variation is required to balance out the centrifugal acceleration of the rotating liquid water. However, the water near the bottom of the cup cannot move as freely because the water adjacent to the bottom sticks to the bottom (that is, the water moves much more slowly near the bottom because of friction or viscous effects). The water touching the wall does not move at all (this is the no-slip boundary condition that occurs in flows of viscous fluids). As a consequence of fluid friction, the angular momentum of the water near the bottom is not enough to oppose the effect of the radial pressure field created by the rotating water away from the bottom boundary layer; in fact the pressure variation is such as to push the water near the bottom of the cup towards the center. Because mass is conserved in this flow, the water that is caused to move towards the center of the cup turns upward towards the surface. Subsequently, it turns towards the side wall at the surface and finally moves down towards the bottom boundary layer replenishing the water that was originally there. This circulatory pattern of motion is the secondary motion (that can be viewed in a meridian plane). The primary motion is, of course, the circulatory motion initially induced by stirring with the spoon.

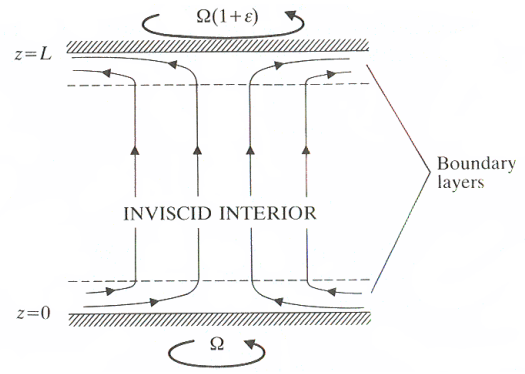

Figure 5: The secondary flow between differentially rotating boundaries [2]. The secondary flow is completed due to an outer wall that is not shown here. At that wall the upper part of secondary flow turns downwards and than towards the centre of the bottom disk.

We have seen what happens in a rotating fluid in the case of teacup. If we want to describe that motion theoretically, we have to restrict ourselves to a more ideal situation. This is the subject of the next section.

4 Rotating flows controlled by boundary layers

Imagine two disks, one at $z = 0$, the other at $z = L$, rotating about the z-axis with angular velocity Ω and $\Omega(1 + \epsilon)$, respectively (Figure 5). [5] Here, ϵ is small. Between the disks there is a viscous fluid with viscosity η. The fluid at the border moves with it – the so called *no-slip condition*. Between the disks the fluid must somehow achieve the slight change in angular velocity implied by the boundary condition. If the *Reynolds number* $Re = \frac{\Omega L^2}{\nu}$ is large, we expect thin viscous layers on both boundaries and an essentially inviscid "interior" in between which is largely controlled by the boundary layers. In the upper equation ν is *kinematic viscosity* defined as $\nu = \frac{\eta}{\rho}$.

It is convenient to start with the Navier–Stokes equations relative to the frame of reference which rotates at angular velocity $\boldsymbol{\Omega}$.

$$\frac{\partial \boldsymbol{u}}{\partial t} + (\boldsymbol{u} \cdot \nabla)\boldsymbol{u} + 2\boldsymbol{\Omega} \times \boldsymbol{u} + \boldsymbol{\Omega} \times (\boldsymbol{\Omega} \times \boldsymbol{x}) = -\frac{1}{\rho}\nabla p + \nu \nabla^2 \boldsymbol{u} \qquad \nabla \cdot \boldsymbol{u} = 0 \tag{13}$$

Here $\boldsymbol{u}$ denotes the fluid velocity *relative to the rotating frame*, and $\partial \boldsymbol{u}/\partial t$ denotes the rate of change of $\boldsymbol{u}$ at a fixed position $\boldsymbol{x}$ in the frame. The third and fourth term in equation are Coriolis and centrifugal term, respectively. Vector identity

$$\boldsymbol{\Omega} \times (\boldsymbol{\Omega} \times \boldsymbol{x}) = -\nabla \left[\frac{1}{2} (\boldsymbol{\Omega} \times \boldsymbol{x})^2 \right] \tag{14}$$

enables us to clear away the centrifugal term by defining a "reduced pressure" $p_R = p - \frac{1}{2}\rho(\boldsymbol{\Omega} \times \boldsymbol{x})^2$. In the subsequent derivation we shall drop the suffix, but will keep in mind that p denotes reduced pressure.

In our derivation we are interested in relative flows $\boldsymbol{u}$ which are weak compared to the basic rotation of the system as a whole. If we let U denote a typical value of $|\boldsymbol{u}|$, and let L denote a typical length scale of the flow, the dimensionless parameter $U/\Omega L$ will therefore be small (of order ϵ). Now, the term $(\boldsymbol{u} \cdot \nabla)\boldsymbol{u} \approx U^2/L = \epsilon \Omega U$ may be neglected in comparison with the Coriolis term $2\boldsymbol{\Omega} \times \boldsymbol{u} \approx \Omega U$. The equations governing the small departure $\boldsymbol{u}$ from a state of uniform rotation with angular velocity $\boldsymbol{\Omega}$ are then

$$\frac{\partial \boldsymbol{u}}{\partial t} + 2\boldsymbol{\Omega} \times \boldsymbol{u} = -\frac{1}{\rho}\nabla p + \nu \nabla^2 \boldsymbol{u} \qquad \text{and} \qquad \nabla \cdot \boldsymbol{u} = 0. \tag{15}$$

[5] As we will see later on it is the difference in angular velocities that matters. Therefore one of the disks could be kept still.

Within this framework we consider the flow at large Reynolds number $Re = \Omega L^2/\nu$, and we assume the main part of that flow to be essentially inviscid.

4.1 Steady, inviscid flow

Let us take Cartesian coordinates (x, y, z) fixed in the rotating frame with the z-axis parallel to the rotation axis, so that $\mathbf{\Omega} = (0, 0, \Omega)$. We deduce from equation (15) that a steady, inviscid flow $\boldsymbol{u}_I = (u_I, v_I, w_I)$ satisfies

$$-2\Omega v_I = -\frac{1}{\rho}\frac{\partial p_I}{\partial x} \qquad 2\Omega u_I = -\frac{1}{\rho}\frac{\partial p_I}{\partial y} \tag{16}$$

$$0 = -\frac{1}{\rho}\frac{\partial p_I}{\partial z} \qquad \frac{\partial u_I}{\partial x} + \frac{\partial v_I}{\partial y} + \frac{\partial w_I}{\partial z} = 0. \tag{17}$$

Clearly p_I is independent of z. It follows immediately from equations (16) that v_I and u_I are independent of z also. Moreover, on substituting equations (16) into the right expression of (17) we see that

$$\frac{\partial w_I}{\partial z} = 0. \tag{18}$$

It follows that $\boldsymbol{u}_I$ *is independent of* z. [6] This far reaching result is known as *the Taylor–Proudman theorem.*

4.2 Ekman boundary layer

Let us now turn to the particular problem of steady flow between two differentially rotating (rigid) disks at $z = 0$ and $z = L$ (Figure 5).

If R is large, the flow in the 'interior' will be essentially inviscid, and therefore subject to Taylor–Proudman theorem, but there will be thin viscous layers on both disks.

Consider the boundary layer on $z = 0$. If we assume, in the normal way, that variations of $\boldsymbol{u} = (u, v, w)$ with z are much more rapid than those with x or y, [7] we find that equations (15) reduce to

$$-2\Omega v = -\frac{1}{\rho}\frac{\partial p}{\partial x} + \nu\frac{\partial^2 u}{\partial z^2} \qquad 0 = -\frac{1}{\rho}\frac{\partial p}{\partial z} + \nu\frac{\partial^2 w}{\partial z^2}, \tag{19}$$

$$2\Omega u = -\frac{1}{\rho}\frac{\partial p}{\partial y} + \nu\frac{\partial^2 v}{\partial z^2} \qquad 0 = \frac{\partial u}{\partial x} + \frac{\partial v}{\partial y} + \frac{\partial w}{\partial z}. \tag{20}$$

From the last equation we deduce that w is much smaller than the velocity component parallel to the boundary which leads to the conclusion that p is essentially a function of x and y only. Thus $\frac{\partial p}{\partial x}$ and $\frac{\partial p}{\partial y}$ take on throughout the boundary layer their inviscid 'interior' values, which are given in terms of the interior flow components $u_I(x, y), v_I(x, y)$ by equations (16). The boundary layer equations then become

$$-2\Omega(v - v_I) = \nu\tfrac{\partial^2 u}{\partial z^2}, \tag{21}$$

$$2\Omega(u - u_I) = \nu\tfrac{\partial^2 v}{\partial z^2}, \tag{22}$$

and these can be integrated immediately. We make use of the same trick we used in paragraph 2; we multiply the second equation by i and add the results to the first, whence

$$\nu\frac{\partial^2 f}{\partial z^2} = 2\Omega i f, \tag{23}$$

where

$$f = u - u_I(x, y) + i[v - v_I(x, y)]. \tag{24}$$

[6] I have to emphasize that this does not mean also $w_I = 0$; w_I can have some constant value.

[7] For this and other approximations in subsequent derivation consult [2], pp. 266-267.

The general solution is again

$$f = A\exp[-(1+i)z'] + B\exp[(1+i)z'], \tag{25}$$

where $z' = (\Omega/\nu)^{1/2}z$, and A and B are arbitrary functions of x and y. To match with the interior flow we require $f \to 0$ as $z' \to \infty$, so $B = 0$. As the rigid boundary $z = 0$ is at rest in the rotating frame, we require $u = v = 0$ there, so

$$f = -(u_I + iv_I)\exp[-(1+i)z'], \tag{26}$$

which implies

$$u_E = u_I - \exp[-z'](u_I\cos z' + v_I \sin z'), \tag{27}$$

$$v_E = v_I - \exp[-z'](v_I\cos z' - u_I \sin z'). \tag{28}$$

At the 'edge' of this *Ekman boundary layer*, where the flow matches with that in the interior, there is a small, but highly significant, z-component of velocity. To see this, note that

$$\begin{aligned}\sqrt{\frac{\Omega}{\nu}}\frac{\partial w}{\partial z'} &= \frac{\partial w}{\partial z} = -\left(\frac{\partial u}{\partial x} + \frac{\partial v}{\partial y}\right) = \\ &= \left(\frac{\partial v_I}{\partial x} - \frac{\partial u_I}{\partial y}\right)\exp[-z']\sin z' - \left(\frac{\partial u_I}{\partial x} + \frac{\partial v_I}{\partial y}\right)(1 - \exp[z']\sin z').\end{aligned} \tag{29}$$

Now, the final term vanishes by virtue of equations (16), so on integrating with respect to z' from $z' = 0$ to $z' = \infty$ we find the value of w at the edge of the Ekman layer to be

$$w_E(x,y) = \frac{1}{2}\sqrt{\frac{\nu}{\Omega}}\left(\frac{\partial v_I}{\partial x} - \frac{\partial u_I}{\partial y}\right). \tag{30}$$

This expression may be written

$$w_E(x,y) = \frac{1}{2}\sqrt{\frac{\nu}{\Omega}}\omega_I, \tag{31}$$

where ω_I is the z-component of the vorticity of the interior flow. [8]

If the (bottom) disk is rotating with angular velocity Ω_b relative to the rotating frame, the above expression generalizes to

$$w_E(x,y) = \sqrt{\frac{\nu}{\Omega}}\left(\frac{1}{2}\omega_I - \Omega_b\right). \tag{32}$$

Similarly, if Ω_t denotes the angular velocity of a (rigid) upper disk at $z = L$ relative to the rotating frame, than there is a small z-component of velocity up into the boundary layer on $z = L$ of

$$w_E(x,y) = \sqrt{\frac{\nu}{\Omega}}\left(\Omega_t - \frac{1}{2}\omega_I\right). \tag{33}$$

4.3 Determination of the 'interior' flow

We are now in a position to determine the flow in the inviscid interior of the fluid. The argument is beautifully simple: the components u_I, v_I and w_I are all independent of z, so $\omega_I = \partial v_I/\partial x - \partial u_I/\partial y$ and w_I are independent of z. The expressions (32) and (33), valid at the top of the lower boundary layer and the bottom of the upper boundary layer respectively, must therefore match. So

$$\frac{1}{2}\omega_I - \Omega_b = \Omega_t - \frac{1}{2}\omega_I,$$

that is

$$\omega_I = \Omega_t + \Omega_b.$$

[8] Vorticity is defined as $\omega = \nabla \times \boldsymbol{u}$, where $\boldsymbol{u}$ is fluid velocity.

In the case of Figure 5, with $\Omega_b = 0$ and $\Omega_t = \Omega\epsilon$, this gives

$$\omega_I = \frac{\partial v_I}{\partial x} - \frac{\partial u_I}{\partial y} = \Omega\epsilon.$$

At this point it is convenient to switch to cylindrical polar coordinates, and on assuming that the velocity field is axisymmetric we find

$$\frac{1}{r}\frac{\mathrm{d}}{\mathrm{d}r}(ru_{\theta I}) = \Omega\epsilon.$$

The solution of this which is finite at $r = 0$ is

$$u_{\theta I} = \frac{1}{2}\Omega\epsilon r,$$

so the fluid in the interior rotates at an angular velocity, which is the mean of those of the two boundaries. This behaviour is a direct result of the influence of the top and bottom boundary layers.

The solution in the interior is completed by returning to equation (30) to obtain

$$u_{zI} = \frac{1}{2}\sqrt{\nu\Omega}\epsilon,$$

and then turning to the incompressibility condition

$$\frac{1}{r}\frac{\partial}{\partial r}(ru_{rI}) + \frac{\partial u_{zI}}{\partial z} = 0$$

in the interior, which gives $u_{rI} = 0$. The secondary flow in the interior is therefore purely in the z-direction (Figure 5).

5 Rotating disks experiment

In order to investigate the fluid flow in rotating frames, researchers performed various experiments. The basic idea is that the (viscous) fluid is confined between two rotating disks. In general case two boundary layers may be present. [9] The problem is that the equations of motion are so complex, that no exact solutions are known for this problem even in the stationary regime (one disk fixed the other rotating). Therefore scientist have to make use of numerical simulations and various experiments to shed light on the physical mechanisms going on in the rotating fluid. [10]

5.1 Experimental set-up

In order to study the flow between two rotating disks the experimental set-up shown in Figure 6 was built. The cell consists of a cylinder of small height h closed by a top disk and a bottom disk, both of radius $R = 140$ mm. The upper disk is made of glass and rotates together with the cylindrical sidewall which is made of PVC. The reason why the cylinder and top disk are made of PVC and glass is to allow visualization from above and from side. The bottom disk is made of rectified brass, with a black coating to improve visualization contrast. To allow the differential rotation the radius of the bottom disk is slightly smaller (a tenth of millimeter) than the radius of the shrouding cylinder. The thickness h of the cell can be varied between few mm up to several cm.

[9] This problem gave rise to a famous controversy in the history of fluid mechanics: George Batchelor (1951) argued that two boundary layers, separated by a solid body rotation core, must take place in the fluid, whereas Keith Stewartson (1953) claimed that only one boundary layer should be present. It has actually been shown, many years later, that a large variety of solutions may coexist in this flow, including the ones of Batchelor and Stewartson.

[10] In this section the focus is not on the recirculation (teacup) flow but rather on the instability patterns in rotating fluids.

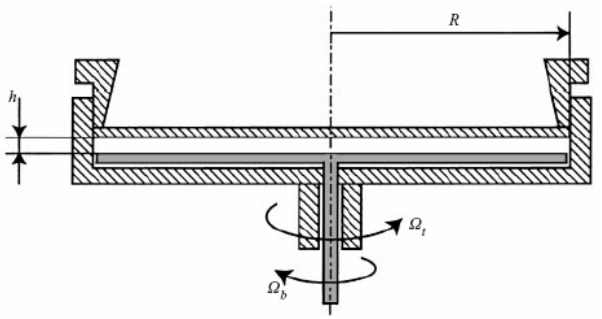

Figure 6: Sketch of the experimental set-up [6].

The cell is filled with a mixture of water, glycerol and small anisotropic flakes. The latter enable us to visualize the fluid flow. The flakes' orientation with the fluid leads to variations of the reflected light. For example, if the flakes are mainly horizontal, they reflect light, if they are vertical they do not reflect it so well. The kinematic viscosity $\nu = \eta/\rho$, where η is viscosity and ρ density of the fluid, lies between $1 \cdot 10^{-6} < \nu < 8 \cdot 10^{-6}$ m^{2}s^{-1} due to different concentration of glycerol.

Each of two disks rotate with its own angular velocity Ω_i, where index $i = b, t$ stands for bottom and top disk respectively. Angular velocities of the disks range from 0 to 10 rad/s but the upper disk rotates anticlockwise only, whereas the bottom one can rotate clock- or anticlockwise. Anticlockwise rotation is taken positive. We call *co-rotation* the situation where both disks rotate in the same direction (Ω_b and Ω_t are of the same sign) and *counter-rotation* when the disks rotate in the opposite directions (they have opposite signs). If one of the disks is left fixed, the other rotating, the regime is called *rotor-stator regime*.

We will define some dimensionless numbers that describe our cell. The first is *radius-to-height ratio* defined as $\Gamma = \frac{R}{h}$, where R is radius and h height of the cell. The second number is *Reynolds number* $Re_i = \frac{\Omega_i h^2}{\nu}$, where index $i = b, t$ denotes the bottom and top disk respectively, Ω_i is the angular velocity of the disks and ν the kinematic viscosity. The last number is *rotation ratio* defined as $s = \frac{\Omega_b}{\Omega_t} = \frac{Re_b}{Re_t}$.
Rotation ratio is positive ($s > 0$) in the co-rotation regime and negative ($s < 0$) in the counter-rotation regime.

5.2 Recirculating flow

Each rotation is associated with a meridian recirculating flow, which can be inward or outward depending on the rotation ratio. For arbitrary positive and small negative rotation ratio s, the radial recirculating flow is roughly the same as in the rotor-stator case ($s = 0$): it consists of an outward boundary layer close to the faster disk and an inward boundary layer close to the slower disk. At small negative rotation ratio the centrifugal effect of the slower disk is not strong enough to counteract the inward flow from the faster disk. But as the rotation ratio s is decreased below -0.2, the slower disk induces a centrifugal flow too, and the radial recirculating flow appears to come organized into two-cell recirculating structure as shown in Figure 7, 8. [11] At the interface of these two cells a strong shear layer takes place. The centrifugal flow induced by the faster disk recirculates towards the centre of the slower disk due to the lateral endwall. This inward recirculation flow meets the outward radial flow induced by the slower disk, leading to a stagnation circle where the radial component of the velocity vanishes.

[11] PIV is acronym for Particle Image Velocimetry. Small particles (≈ 10 μm in diameter) seeding the flow are used as a tracer and illuminated by laser pulses. Images are acquired with camera synchronized with the laser pulses.

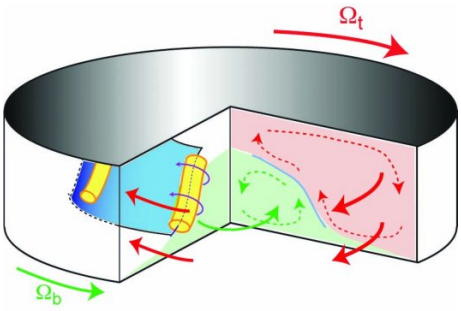

Figure 7: Two cell recirculating flow. Solid red arrows show primary motion (azimuthal flow), dotted arrows show secondary motion (recirculation flow) in the cell [8].

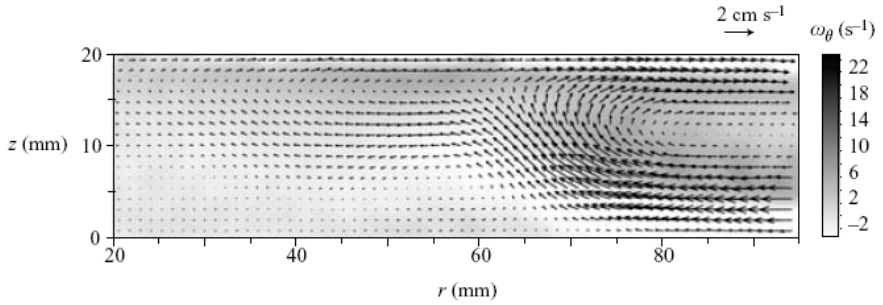

Figure 8: Experimental velocity field of the base flow in the meridian plane made by PIV measurements. Note that only the region $0.14 \leq r/R \leq 0.68$ is shown [7].

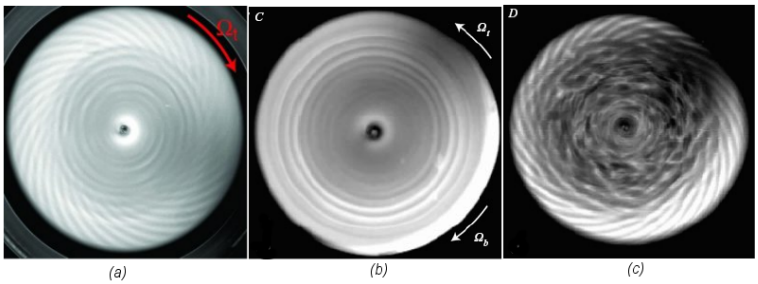

Figure 9: Mixing of axisymmetric propagating vortices C and positive spirals S^+ (a), propagating circular vortices C (b) and disordered flow D [6].

5.3 Instability flow patterns

We now turn to the instability patterns of the flow between two rotating disks close to each other ($\Gamma = 20.9$), in both co- and counter-rotating flows.

For $s \geq 0$ (rotor-stator or co-rotation) and Re_b fixed, on increasing Re_t, propagating circular structures are first observed. They are shown in Figure 9 (b). These axisymmetric vortices appear close to the cylindrical wall, propagate towards the center and disappear before reaching the center of the cell. Above a secondary threshold of Re_t, spiral structures appear at the periphery of the disks, and circles remain confined between two critical radii (Figure 9 (a)). These spirals are called positive spirals (denoted S^+) since they roll up to the center in the direction of the faster disk (here the top one). Increasing Re_t further, positive spirals progressively invade the whole cell. Still increasing Re_t, the flow becomes more and more disordered (denoted D, Figure 9 (c)).

From Figure 12 we can see that co-rotation shifts upwards the instability thresholds for circles and positive spirals. However, threshold line for circles is parallel to the solid body rotation ($\Omega_b = \Omega_t$) indicating that the angular velocity difference $\Delta\Omega = \Omega_t - \Omega_b$ is the only control parameter of this instability and no influence of the global rotation occurs. By contrast, the borderline for the positive spirals has a larger slope than the solid body rotation line; in this case the relative angular velocity $\Delta\Omega$ is not the only control parameter and an extra velocity of the upper disk is needed for the spirals to arise. The global rotation in this case has a stabilizing effect.

For $s < 0$ (counter-rotating case) the onset of the instability patterns depends on the Reynolds numbers of both disks. For low bottom Reynolds number, $-11 < Re_b < 0$, on increasing the Reynolds number of the upper disk, the appearance of the instability patterns is the same as in the rotor-stator or co-rotation case: axisymmetric propagating vortices, positive spirals and disorder.

But, for $-18 < Re_b < -11$, spirals of a new kind appear on increasing Re_t. These spirals are said to be negative (and denoted S^-) since they now roll up to the centre in the direction of the slower counter-rotating disk (Figure 10 (a)). Unlike circles and positive spirals, negative spirals extend from the periphery to the center – they invade the whole cell. Also, the onset time for negative spirals is much longer than for positive ones or circles; when the onset is carefully approached from below, the growth time of negative spirals can exceed 15 minutes which strongly contrasts circles and positive spirals which appear almost instantaneously. [12]

Increasing Re_t further, positive spirals appear as well at the periphery of the disk, as can be seen in Figure 10 (b). Here negative and positive spirals seem to coexist without strong interaction, which indicates the difference in their origin. The circles and positive spirals have their origin in the boundary layer instability whereas negative ones, on the other hand, originate from shear layer instability.

Still increasing Re_t, negative spirals disappear and positive spirals alone remain (Figure 10 (c)).

Increasing Re_t yet further, circles appear as in the co-rotation case. Still increasing Re_t, the structures become disorganized and the flow becomes turbulent. For $Re_b < -18$ the negative spirals described above become wavy, the flow is more and more disorganized and continuously becomes

[12] Further from the threshold growth time of negative spirals takes more reasonable values (≈ 1 min or few s). Actually, it can be shown that this growth time diverges as one approaches the onset.

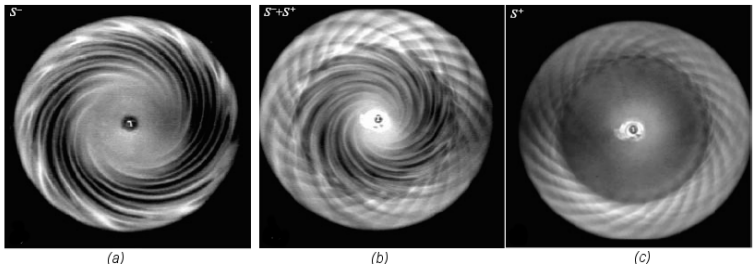

Figure 10: Negative spirals S^- (a) and mixing of positive and negative spirals (b). Positive spirals left after the negative ones faded away (c) [6].

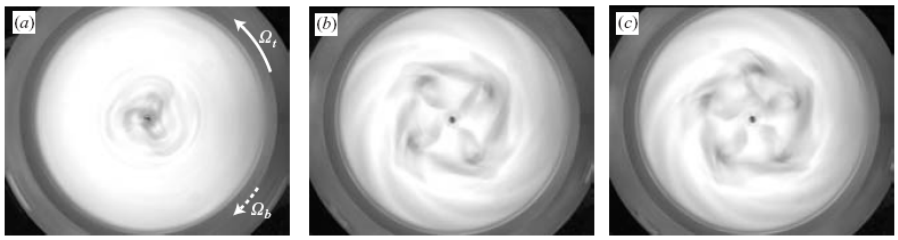

Figure 11: Instability pattern for smaller Γs ($\Gamma = 6.1, 7, 7$ from left to right) [7].

turbulent without a well-defined threshold. Depending on the Reynolds number, the disorder can be generated first at the periphery or in the center and then invades the entire cell.

Up to now our instability patterns were limited to radius-to-height ratio $\Gamma = 20.9$. Does anything changes if one changes it? Researchers enlarged the gap h between the disks (Γ diminishes) and observed a new pattern that consisted of a sharp-cornered polygon of m sides, surrounded by a set of $2m$ outer spiral arms, as can be seen on Figure 11. These polygons arise only for small Γs (less than approx. $\Gamma = 10$). For higher values the vertical confinement leads to a saturated pattern where inner arms, connecting the corners of the polygon to the center of polygons, turn into negative spirals.

Another interesting property of the patterns is that they are not fixed but rather rotate as a whole. Therefore we define the *azimuthal phase velocity* ω_ϕ in the laboratory frame. It corresponds to the angular velocity of the global rotation of the spiral pattern. For the S^+ spirals ω_ϕ is always positive (anticlockwise), i.e. the positive spirals rotate in the direction of the faster (top) disk, regardless of motion of the bottom one. S^- spirals, on the other hand change sign of ω_ϕ. It means that for small Re_t the pattern rotates in the direction of the slower (bottom) disk while at higher Re_t it moves with the top (faster) disk. Here I only compare the directions of the disks and phase velocity. The size of phase velocity is only a fraction of the disk velocities.

The domains of existence of all these patterns are summarized in the regime diagram on Figure 12. We see that the co-rotation flow ($Re_b > 0$, right-hand part of the diagram) is qualitatively the same as the rotor-stator flow (vertical line $Re_b = 0$); the thresholds of instabilities (circles C and positive spirals S^+) are found to increase just with the bottom Reynolds number. By contrast, the counter-rotating case ($Re_b < 0$, left-hand part) is much more rich.

5.4 Numerical description of the patterns

In order to obtain further insight into the instability mechanism of the counter-rotating flow, scientists performed PIV measurements and numerical simulations. On the left part of Figure 13 you can see the horizontal velocity and the associated vertical vorticity field, measured by PIV at mid-height $z = h/2$ for $\Gamma = 7$. Left part of Figure 13 shows the axisymmetric base flow (a)

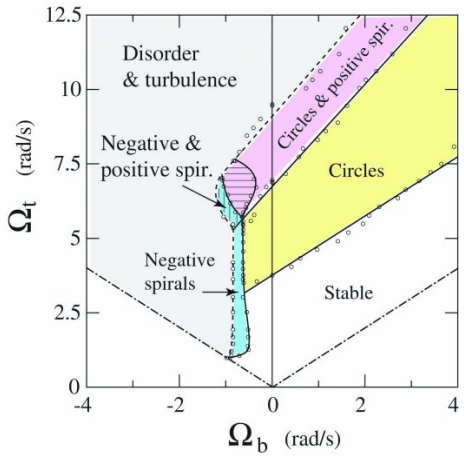

Figure 12: Regime diagram of the rotating disk flow for the aspect ratio $\Gamma = 20.9$ (thickness $h = 6.7$ mm). The right part corresponds to the co-rotation case ($\Omega_b > 0$), the left side to the counter-rotation case ($\Omega_b < 0$), the vertical line denotes the rotor-stator case ($\Omega_b = 0$). The continuous lines define the domain limits, while the dashed give a rough estimate of the disorder transition [8].

while other pictures on the left side show polygonal deformed flow. In order to gain deeper insight in the structure of flow scientists also made numerical simulations. You can see computed axial vorticity field at $z = h/2$ for $\Gamma = 21$ on the right side of Figure 13. Only the inner spirals can be seen in numerical simulations, suggesting that the outer spirals are outside the mid-height plane. The three-dimensional structure can be inferred from numerical vorticity and velocity fields. It is remarkable that the locations of the vorticity extremes approximately coincide for each field, suggesting that the flow structure is roughly invariant along the vertical direction, except close to the disks where boundary layers occur. Along these columnar vortices strong upward flow is present, which advects negative vorticity from the bottom to the top disk.

To find out how the nonlinear differential equations depend on the initial condition two computations were performed for the same flow parameters ($\Gamma = 3, Re_t = 280$), which differ only by the initial condition. The axisymmetric stable flow for $Re_b = 70$ is taken as the initial condition for the fist computation where Re_b was suddenly increased from 70 to a value above the threshold. For the second computation, the bottom Reynolds number was gradually increased from 70 to 80 in four steps, waiting for the saturation of the flow at each step. While the first computation showed a mode $m = 5$ the second one showed a mode $m = 4$. For similar values of Re_b the experiment shows a mixed state of modes 4 and 5. These observations clearly illustrate the sensitivity of the observed pattern to the initial condition. They are in good agreement with a number of experimental observations, where strong hysteresis is observed for the modes, although no hysteresis is present in the value of threshold.

6 Conclusion

Fluid dynamics is one of the most intriguing parts of physics. Why? One part of the answer is that the equations are well established but we are still not able to solve them, except for some very simplified (and unreal) cases. The other part is that we have everyday contact with fluids and their flow, we are fascinated by their complexity and beauty.

In my seminar I presented some examples of fluid flow in rotating frames. One can see that they are impossible to describe mathematically and all but simple and intuitive. Nevertheless modern computers, capable of heavy computations, offer new and exciting perspectives in their understanding. In this context, the excellent recent agreements between experiments and numerical simulations are encouraging.

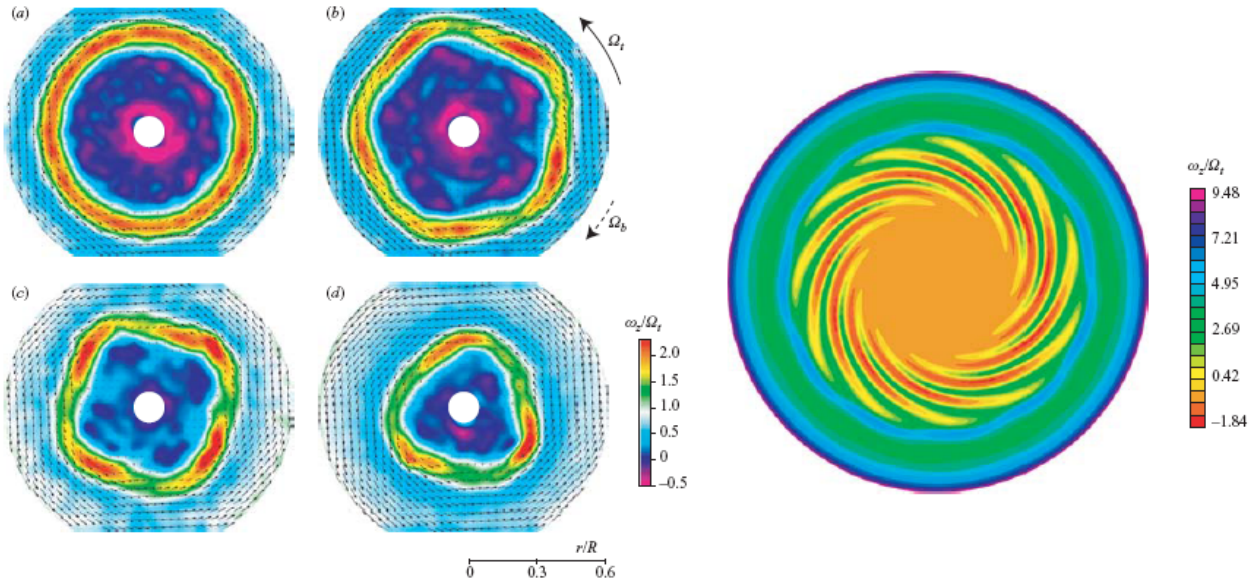

Figure 13: *Left*: Experimental velocity and vorticity fields at mid-height $z = h/2$ for $\Gamma = 7$. First picture (a) is below the onset of instability. *Right*: Numerical axial vorticity field ω_z at mid-height for $\Gamma = 21$ showing a mode $m = 11$. Only the central region $r \leq 0.95R$ is shown [7].

The study of fluid motion in rotating environments is very important in large-scale meteorology and oceanography where the Coriolis effect has to be taken into account. [13]

Study of swirling flows is also of great importance in a number of industrial or practical applications. Hard disk drives are an important example: the instabilities of the thin air layer over the rapidly rotating platters induce vibrations of the read/write heads, that may damage the platters' surface. This type of involvement was especially actual at the time of *Bernoulli disks*. They worked on the Bernoulli principle. When the disk is spinning the air drags it close towards the read/write heads (50μm for the Bernoulli Box). But because the head doesn't actually touch the disk, there are fewer chances for magnetic head crashes. Also, since the disk is closely (but safely) aligned with the magnetic head, more data can be stored and accessed, since the head can accurately read/write from more tracks than otherwise possible.

Another point of practical interest are the turbo machines used in power plants or aeronautics engineering. This latter application involves huge rotation rates (more than 10000 rpm) and accurate modelling of the turbulent phenomena present at small scales are clearly needed for such numerical simulations.

Last but not least the study of swirling flows is interesting because of all the beauty it possesses. Or, as R.P.Feynman put it: "But the real reason is that the subject is enjoyable, and although we humans cut up nature in different ways, and we have different courses in different departments, such compartmentalization is really artificial, and we should take our intellectual pleasure where we find them." [14]

[13] One interesting consequence of rotating Earth are super tankers. They are long enough (more than 300m) to feel the Earth's rotation. When travelling north in the Northern Hemisphere their direction deviates to the west unless compensated.

[14] R.P. Feynman, R.B. Leighton and M. Sands: *The Feynman Lectures on Physics*, Vol. I (Addison Wesley, Reading, Mass. 1963), pp.22-1.

References

[1] R. Podgornik: *Mehanika kontinuov* (study material)

[2] D.J. Acheson: *Elementary fluid dynamics* (Oxford University Press, 1996)

[3] P. Prelovšek: *Geofizika* (study material)

[4] T.E. Faber: *Fluid Dynamics For Physicists* (Cambridge University Press, 1995)

[5] G. Neumann, W.J. Pierson Jr.: *Principles of physical oceanography.* (Prentice-Hall, 1966)

[6] G. Gauthier, P. Gondret, F. Moisy and M. Rabaud: *Instabilities in the flow between co- and counter-rotating disks* (article in J. Fluid Mech. (2002), vol 473, pp. 1-21)

[7] F. Moisy, O. Doaré, T. Pasutto, O. Daube and M. Rabaud: *Experimental and numerical study of the shear layer instability between two counter-rotating disks* (article in J. Fluid Mech. (2004), vol. 507, pp. 175-202)

[8] F. Moisy, T. Pasutto, G. Gauthier, P. Gondret and M. Rabaud: *Spiral patterns in swirling flows* (article in Europhysics News (2003), vol. 34, no. 3)

[9] *http://www.seds.org/messier/m/m100.html*

[10] *http://meted.ucar.edu/hurrican/strike/text/htc_t3.htm*

[11] *http://oceanworld.tamu.edu/resources/ocng_textbook/chapter09/chapter09_02.htm*

[12] *http://people.clarkson.edu/ space/teacup.html*